CYCLIC FRACTURE SIMULATION FRAMEWORK FOR MODELING COLLAPSE IN STEEL STRUCTURES

David A. Padilla-Llano, Ph.D.[1], Jerome F. Hajjar, Ph.D.[2], P.E., Matthew R. Eatherton, Ph.D., S.E.[3], and Benjamin W. Schafer, Ph.D., P.E.[4]

ABSTRACT

Collapse and failure of steel structures subjected to extreme loads, such as seismic forces, is usually preceded by large inelastic deformations and fracture in steel components and connections. However, it has not been common in prior work to include direct simulation of fracture in the performance assessment of structures. In this work, a framework is proposed for cyclic fracture simulation in steel components and connections with application to predict failure and collapse of steel structures. The proposed framework couples a plasticity model for large deformations that captures plastic work stagnation and Bauschinger effect, with a continuum damage model to capture fracture initiation, propagation, and failure through an element elimination strategy. The damage model includes the effects of non-proportional loading and strain history. Calibration of the model parameters is discussed for common structural steels and weldments using typical material tests. Validation of the framework against monotonic and cyclic tests ranging from ancillary material tests to components and subassemblies shows that the model is capable simulating the experimentally observed fracture patterns and failure progression. The proposed framework provides a valuable tool for simulating three-dimensional steel structures subjected to extreme loads including collapse triggered by fracture in components and connections.

[1]Research Assoc., Civil & Env. Engineering, Northeastern University, Boston, MA d.padillallano@northeastern.edu
[2]Chair and Professor, Civil & Env. Engineering, Northeastern University, Boston, MA jf.hajjar@northeastern.edu
[3]Professor, Civil & Env. Engineering, Virginia Tech, Blacksburg, VA meather@vt.edu
[4]Professor, Civil Engineering, The Johns Hopkins University, Baltimore, MD schafer@jhu.edu

Cyclic Fracture Simulation Framework for Modeling Collapse in Steel Structures

David A. Padilla-Llano, Ph.D.[1], Jerome F. Hajjar, Ph.D.[2], P.E.,
Matthew R. Eatherton, Ph.D., S.E.[3], and Benjamin W. Schafer, Ph.D., P.E.[4]

ABSTRACT

Collapse and failure of steel structures subjected to extreme loads, such as seismic forces, is usually preceded by large inelastic deformations and fracture in steel components and connections. However, it has not been common in prior work to include direct simulation of fracture in the performance assessment of structures. In this work, a framework is proposed for cyclic fracture simulation in steel components and connections with application to predict failure and collapse of steel structures. The proposed framework couples a plasticity model for large deformations that captures plastic work stagnation and Bauschinger effect, with a continuum damage model to capture fracture initiation, propagation, and failure through an element elimination strategy. The damage model includes the effects of non-proportional loading and strain history. Calibration of the model parameters is discussed for common structural steels and weldments using typical material tests. Validation of the framework against monotonic and cyclic tests ranging from ancillary material tests to components and subassemblies shows that the model is capable simulating the experimentally observed fracture patterns and failure progression. The proposed framework provides a valuable tool for simulating three-dimensional steel structures subjected to extreme loads including collapse triggered by fracture in components and connections.

Introduction

Collapse of steel structures subjected to extreme loads, such as seismic forces, is usually preceded by large inelastic deformations and fracture in components and connections. Cases of damaged structures such as the Alexander Kielland drilling rig in 1980 [1] and the fractures in steel buildings during the 1994 Northridge and 1995 Kobe earthquakes [2,3] highlight the importance of including fracture simulation in the performance assessment of steel structures under extreme loading. In recent years, models to simulate the fracture in steel structures have been proposed including some popular approaches such as the traditional linear elastic (LEFM) and elastic-plastic fracture

(EPFM) models, the void growth-coalescence based models (e.g., [4,5,6]), the extended finite elements models (XFEM). Simulating accurately the behavior of steel structural systems where damage localization and fracture may occur at several locations requires a strategy that generally involves fine-grained computational finite element meshes. This poses limitations on the type of models used where computational time and accuracy of the simulated fracture process are competing factors that limit the options to widely include fracture analyses. In this paper a framework is proposed for modeling plasticity and cyclic fracture in steel components. The framework implements a continuum damage-plasticity model for large deformations that accounts for the effects of stress triaxiality, Lode angle, non-proportional loading, strain history effects, and fracture energy dissipation. An element deletion strategy is adopted to simulate fracture propagation. The proposed framework enables to explicitly simulate localized damage and fracture in components and connections that can trigger collapse steel structures and buildings using mesh densities that are typical of high-fidelity structural analyses.

Cyclic Fracture Model

In this paper, the process that leads to fracture in the context of finite elements is implemented using a hybrid approach that combines a coupled damage-plasticity model and an element deletion strategy to simulate the loss of load-carrying capacity due to fracture. The Yoshida-Uemori (YU) plasticity model [7] is coupled with a damage model to simulate the material plastic stress-strain response. The YU model can describe the large-strain cyclic behavior in metals including isotropic and kinematic hardening, the Bauschinger effect, and plastic work stagnation. In addition, the YU model ensures stabilization of the plastic hardening during cyclic loading with constant strain amplitudes [8], a drawback present in popular plasticity models with combined kinematic-isotropic hardening (e.g., the Lemaitre-Chaboche model [9]). The damage leading to fracture is assumed here as the material's *loss of deformation capability,* and it is considered a *self-similar process on any deviatoric proportional path* for any hydrostatic pressure [10]. The nonlinear history based damage evolution proposed by Wen-Mahmoud [11] is used as a template to implement the damage leading to fracture initiation, and an enhanced version of the Hillerborg's [12] approach is proposed to simulate the softening due to crack opening on the material response. Each part of the proposed model are described next.

Cyclic Coupled Damage-Plasticity Model for Large Plastic Strains

The Yoshida-Uemori plasticity model [7] employs three coupled surfaces to describe the large-strain cyclic behavior of metals. A constant-size yield surface is coupled with a bounding surface to control the isotropic and kinematic hardening. The yield surface experiences only kinematic hardening and describes the Bauschinger effect seen during loading reversals. The overall plastic hardening is represented by the isotropic hardening of the bounding surface. A third strain-based memory surface together with the kinematic hardening of the bounding surface simulate the plastic-work hardening stagnation and yield plateau. The three surfaces are described by:

$$f_Y(\sigma, \alpha) = \left[\frac{3}{2}(S - \alpha):(S - \alpha)\right]^{1/2} - \sigma_{yo}(1 - \omega) = 0 \qquad \text{(yield surface)} \qquad (1a)$$

$$f_B(\sigma, \beta) = \left[\frac{3}{2}(S - \beta):(S - \beta)\right]^{1/2} - R(1 - \omega) = 0 \qquad \text{(bounding surface)} \qquad (1b)$$

$$g_\varepsilon(\varepsilon_p, q) = \left[\frac{2}{3}(\varepsilon_p - q):(\varepsilon_p - q)\right]^{1/2} - r = 0 \qquad \text{(memory surface)} \qquad (1c)$$

where S= deviatoric stress tensor, α= yield surface center, σ_{yo}= yield surface size, β= bounding surface center, R= bounding surface size, ω= damage variable to control the strain-stress response

softening due to fracture, ε_p= plastic strain tensor, q= memory surface center, and r= memory surface size. The kinematic hardening of both yield and bounding surfaces is coupled through the backstress $\theta=\alpha-\beta$ which describes the relative kinematic motion of the yield surface respect to the bounding surface. The evolution rules of β and θ are defined as:

$$d\theta = \frac{2}{3}(aC)d\varepsilon_p - C(a/\bar{\theta})^{1/2}\theta d\varepsilon_p \tag{2a}$$

$$d\beta = \frac{2}{3}(mb)d\varepsilon_p - m\beta d\varepsilon_p \tag{2b}$$

where $\bar{\varepsilon}_p$= equivalent plastic strain; $a = R-\sigma_{yo}$; $\bar{\theta} = [(3/2)\theta:\theta]^{1/2}$; and C, b and m are model parameters. The bounding surface size R is a function of the equivalent plastic strain and has an initial size $R_o>\sigma_{yo}$. The evolution rule for R is defined by:

$$dR = (mR_{sat}e^{-m\bar{\varepsilon}_p} + m_l)\,d\bar{\varepsilon}_p \tag{3}$$

which is the rule proposed by Zaverl and Lee [13] plus an additional linear hardening term m_l introduced in [8] to account for trends experimentally observed in which the true stress does not saturates but continue increasing approximately linearly at large plastic strains.

The memory surface proposed by Ohno [14] is adopted to memorize the hardening history and determine the non-isotropic hardening region of the bounding surface. The latter condition is met when the current plastic strain tensor is inside the memory surface. Thus, $dR = 0$ when $(\varepsilon_p - q):d\varepsilon_p \leq 0$ and $g_\varepsilon(\varepsilon_p, q) < 0$. The evolution of r and q are given by:

$$dr = \frac{2h}{3r}\left(\varepsilon_p - q\right):d\bar{\varepsilon}_p \tag{4a}$$

$$dq = \frac{2(1-h)}{3r^2}\left(\varepsilon_p - q\right):d\bar{\varepsilon}_p \tag{4b}$$

where h is a material parameter. The yield plateau is simulated by assuming an initial memory surface size $r_o = \bar{\varepsilon}_L$ and setting $C=$ and m to $0.001C$ and $0.001m$ for $\bar{\varepsilon}_p \leq \bar{\varepsilon}_L$.

Damage Evolution Model
The damage resulting in fracture is simulated in two stages: the first one corresponds to damage accumulated that triggers fracture initiation, and a second stage, fracture evolution, where the material stress-strain response is weakened due to accumulated damage.

Fracture Initiation Model
The damage accumulation process that triggers fracture initiation is expressed as a function of the equivalent plastic strain and the current stress state. A state variable D_i is introduced to quantify damage up to the point of fracture initiation, where $D_i =0$ for no-damage, and $D_i =1$ at fracture initiation. This variable is not coupled to the plasticity model and its purpose is to indicate when the material stress-strain response starts softening. The incremental form for D_i is

$$dD_i = e^{c_1\kappa} \cdot c_2 \left(\frac{\bar{\varepsilon}_{pt}}{\bar{\varepsilon}_i}\right)^{c_2-1} \cdot \frac{d\bar{\varepsilon}_p}{\bar{\varepsilon}_i} \tag{5}$$

where c_1, c_2 = material constants, $\bar{\varepsilon}_{pt} = [(2/3)\varepsilon_p:\varepsilon_p]^{1/2}$ the transient equivalent plastic strain, $\bar{\varepsilon}_i$ is the fracture initiation strain surface, and κ = the parameter that accounts for the non-proportional and history effects in the damage accumulation process. If $c_1=0$ and $c_2=1$ in Eq. 5, the commonly used linear damage accumulation model is recovered [4,15].

Fracture initiation strain: The fracture initiation strain surface $\bar{\varepsilon}_i$ is given by the expression

$$\bar{\varepsilon}_i = \bar{\varepsilon}_0 \cdot e^{-c_3\eta} \cdot (1 + \gamma|\xi|^{c_4}) \tag{6}$$

with the first term representing the influence of the stress triaxiality $\eta = I_1/3\bar{\sigma}$, and the second term is the contribution of the Lode angle parameter $\xi = 1 - (2/\pi)\cos^{-1}[(27/2)J_3/\bar{\sigma}^3]$, where $\bar{\sigma} = (3J_2)^{1/2}$ is the von Mises stress, and I_1, J_2 and J_3 are the stress tensor invariants. The fracture initiation strain surface is assumed symmetric about the axis defined by $\xi=0$. In Eq. 6 the strain parameter $\bar{\varepsilon}_0$ is the fracture initiation strain for the generalized shear or torsion loading case (i.e. $\eta=\xi=0$), γ is the ratio of fracture strain of the generalized shear loading case ($\xi=0$) to the generalized tension/compression loading case ($\xi=\pm1$), and c_3 and c_4 are material parameters that control the surface's curvature. Fig. 1 illustrates the influence of each parameter in Eq. 6.

Similar formulations for the fracture strain surface have been proposed, for example in [4,5,10,16–18], however the form proposed in Eq. 6 is chosen for its simplicity and because it can represent a large family of surfaces for the fracture strain surface besides the von Mises type ($\gamma=0$ or $c_4=0$). For example, for materials that are more ductile in tension ($\xi=1$) than in shear ($\xi=0$), γ and c_4 can be set to provide a surface with Lode dependency that will reflect such condition like the blue curve on Fig. 1a. Conversely, if a material is more ductile in pure shear than in tension, then the green curve in Fig. 1a or any with $c_4 \geq 0$ in Fig. 1b could be adopted.
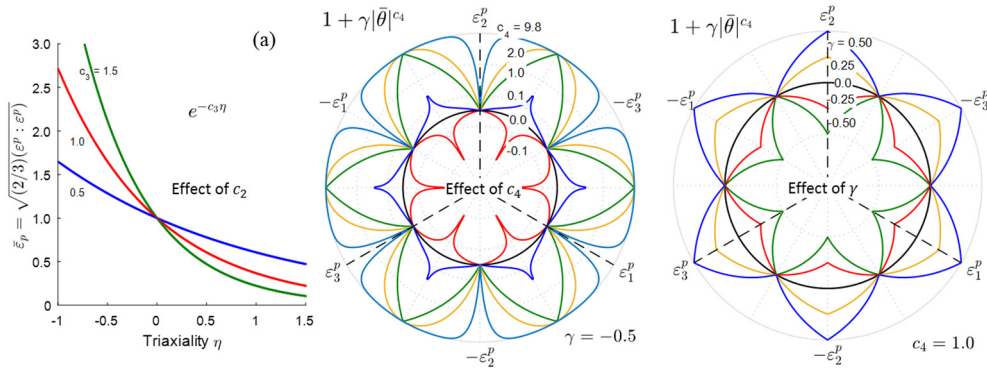

Figure 1. Effects of parameters c_3 (a), c_4 (b) and γ (c) in the fracture initiation strain surface.

Non-proportional loading and history parameter: Parameter κ in Eq. 5 describes the effect on the damage accumulation of the previous non-proportional and cyclic loading history. κ increases or decreases the damage accumulation rate for the cases of cyclic and non-proportional loading. The expression for κ is given by

$$\kappa = \int_0^{\bar{\varepsilon}_p} \chi d\bar{\varepsilon}_p = \int_0^{\bar{\varepsilon}_p} = \text{sign}\left(\Sigma_{i=1}^3 \Sigma_{j=1}^3 \sigma_{ij}\right)\left[1 - \frac{\sigma:\alpha}{\|\sigma\|\|\alpha\|}\right]d\bar{\varepsilon}_p \tag{7}$$

where $\chi \in [-2,2]$ is a parameter that describes the non-proportionality state and changes in loading direction. Both χ and κ are zero for monotonic proportional loading cases and non-zero otherwise. Similar parameters have been proposed in [15 and 11].

Cutoff region: A cutoff region is defined based on the assumption that damage only occurs for stress states with maximum positive principle stresses [11, 19–21]. This assumption states that the increment in the damage variable $dD_i=0$ if $\eta \leq -2/3 \cos[\pi/6(\xi-1)]$. Other definitions for the cutoff region have been proposed in the past (e.g. $\eta \leq -1/3$ [22] or $\eta \leq 0$ [6,23]); however, the proposed limit for η is chosen as it can be used for cases where fracture occurs with negative η and varying ξ as shown in [24,25] and for brittle fracture behavior.

Fracture Evolution Model

The damage process that drives the material strain-stress response softening is set as a function of the material's fracture energy capacity G_f. The assumption is that the material loses load-carrying capacity as fracture plastic work accumulates after fracture initiates. Once the fracture plastic work exceeds G_f, failure of the material is assumed. The fracture energy expression as a function of the characteristic length L_c proposed by Hillerborg [12] is adopted to reduce mesh dependency. Damage after fracture initiation is assumed to increase exponentially with the fracture plastic work, and it is affected by the non-proportional loading history as follows

$$d\omega = \mathcal{H}(D_i - 1) \cdot \frac{\alpha e^{c_1 \kappa}}{1 - e^{-c_5}} \cdot \frac{\bar{\sigma} L_c}{G_f} \cdot e^{-c_5 \int_{\bar{\varepsilon}_i}^{\bar{\varepsilon}_p} (\bar{\sigma} L_c / G_f) d\bar{\varepsilon}_p} \tag{8}$$

where $\mathcal{H}(\cdot)$= Heaviside function; c_5= material parameter, and G_f is a function of the fracture energy for generalized shear or torsion G_{fo}, the stress triaxiality and Lode angle parameter as

$$G_f = G_{fo} \cdot e^{-c_3 \eta} \cdot (1 + \gamma |\xi|^{c_4}) \tag{9}$$

This definition of G_f accounts for the differences in the fracture process when loading in pure tension, pure shear or any other mixed stress state. The damage variable ω is coupled to the YU plasticity model to simulate the material load-carrying capacity loss. When the load-carrying capacity at an integration point is exhausted (ω=1), the integration point is deleted, and once all integration points associated to an element are deleted, the element is removed.

Numerical Integration of the Constitutive Equations

The proposed model is implemented as a user material for ABAQUS [26] using an implicit stress integration algorithm. The backward Euler discretization and the successive substitution method were used together with staggered stress algorithm to integrate the current stress σ_{n+1} as a function of the increments in total strain $d\varepsilon_{n+1}$ and damage $d\omega_{n+1}$ as follows:

$$\begin{aligned}
\sigma_{n+1} &= [1 - \omega_{n+1}] \mathbb{C}^e : \varepsilon_{n+1}^e = \varphi_{n+1} \mathbb{C}^e : [\varepsilon_{n+1} - \varepsilon_{n+1}^p] \\
&= \varphi_n \mathbb{C}^e : [\varepsilon_n^e + d\varepsilon_{n+1}] - \varphi_n \mathbb{C}^e : d\varepsilon_{n+1}^p + d\varphi_{n+1} \mathbb{C}^e : \varepsilon_{n+1}^e
\end{aligned} \tag{10}$$

where $\varphi = 1 - \omega$, $\mathbb{C}^e$= the undamaged elastic isotropic stiffness tensor, and ε^e= total strain tensor elastic part. The first term in Eq. 10 represents an elastic predictor step, while the second and third terms represent plastic and damage corrector steps respectively. In the staggered integration algorithm, first, a trial stress is calculated based on the material status at the n-step, then the plastic correction is performed in the absence of damage evolution ($d\omega_{n+1}$=0) to find $d\varepsilon_{n+1}^p$, and finally the damage correction step is performed under frozen plasticity conditions. An adaptive sub-stepping method was implemented to improve convergence for large strain increments.

Calibration of the Cyclic Fracture Model

Calibration of the proposed model for a particular material is achieved in two steps: (1) calibration of the modified YU plasticity model, and (2) calibration of the fracture initiation and evolution models. Tension and tension-compression cyclic tests using classic tensile coupons, circular notched bars, and/or grooved plate specimens can be used to calibrate the plasticity model. These specimens provide stable monotonic and cyclic responses for large plastic deformations with little variation in η and ξ across the cross-sections within the gage length.

To calibrate the fracture models requires data from fracture tests with specimens that exhibit different stress triaxiality and Lode angles at the fracture point. Fig. 2 illustrates typical

specimens used to characterize fracture and where they fall with respect to their stress triaxiality and Lode angle parameter for monotonic loading. This figure suggests that an ideal specimens set for calibration may include circular and rectangular notched bars, flat grooved plates, and torsional tubes ($\eta=\xi=0$). These specimens can provide enough information to calibrate the proposed model and they are easy to fabricate. Other specimens with wider η and ξ variations can be used, such as the plates with inclined notches and butterfly specimens proposed in [23] and [15] respectively. In the calibration process all model parameters are determined using a global optimization algorithm to minimize the error between the experimental and simulated load-deformation responses. Parameters for structural steels A572 and A992 both Grade 50; weldments E70T6 and E71T8-K6; and A490 bolts were calibrated using specimens similar to those in Fig. 2 from a set of monotonic and cyclic tests reported in [23, 27–31]. The calibrated parameters are used for the validation examples discussed in the next section.
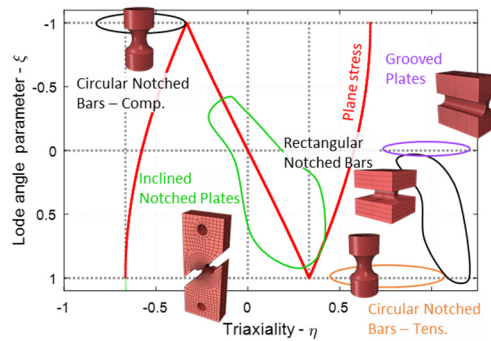

Figure 2. η vs. ξ plane and typical specimens used for fracture characterization.

Validation of the Cyclic Fracture Model

The proposed fracture model was validated against ancillary material tests steel and subassemblies tests under monotonic and cyclic loading. Simulations were carried out using ABAQUS/Explicit to compare to the reported experimental results, specifically the load-deformation response and fracture pattern. Solid continuum elements with reduced integration (C3D8R) were used in the mesh and all relevant specimen and tests setup details were included. The next sections describe the selected tests used for the validation study and the outcomes. The YU plasticity model parameters were calibrated from coupon tests data provided in the corresponding tests reports, while the fracture parameters generally correspond to those calibrated from the data sets described in the previous section. The material parameters used for each validation tests are summarized in Table 1.

Ancillary A572 material test
A set of material tests carried out by Kanvinde et al. [27] were used to validate the fracture parameters for A572 Grade 50 steel. The load-deformation results shown in Fig. 3 show that the cyclic fracture model predicts accurately the softening of the global response due to fracture and the fracture initiation location and propagation patterns for each tests resemble very well that reported in the experiments. For the pull-plate specimen with holes, fracture initiated at the hole surface close to the straight edge side [27]. The same fracture initiation location was observed in the simulations, see Fig. 3a. For the compact tension specimen, fracture started at the notch mid-thickness center and propagated faster in the center than in the region closer to the side surfaces [27]. Similar pattern was observed in the simulations, see Fig. 3b.
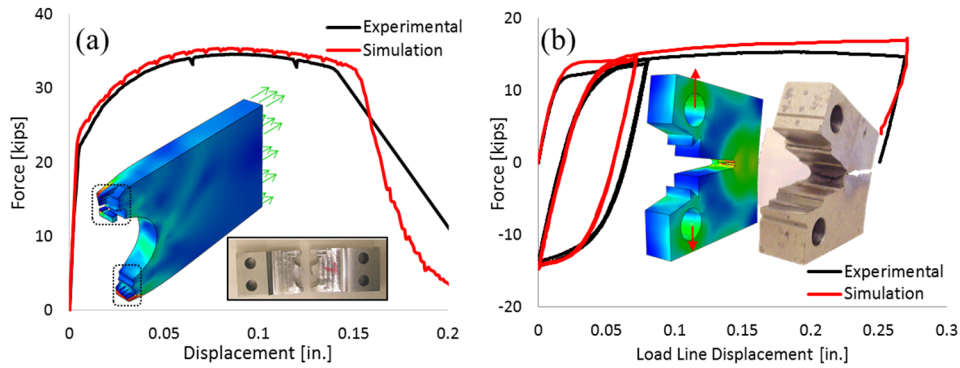
Figure 3. Responses and fracture pattern of selected tests for A572 steel.

NIST Steel Moment Frames with Column Removal

The tests performed by Sadek et al. [32] to evaluate the behavior of steel moment frames in a column removal scenario were used to validate the fracture model. The study considered two moment frames, one with beam-to-column welded connections and reduced beam sections (RBS), and one with welded unreinforced flange-bolted web connections (WUFB). The columns and beams were A992 Grade 50 steel. The bolts used for the WUFB frame were A490 structural bolts, and E70T6 electrodes were used for the welds. Downward displacements were applied to the center column to simulate the collapse under column removal conditions. The load-deformation responses, failure progression, and fracture patterns reported for each tests are captured very well in the simulations. In the RBS specimen, failure was characterized by fracture at the bottom flange reduced section which then propagated through the web as loading progressed [32], see Fig. 4a. Failure for the WUFB specimen started with local buckling of the beam top flanges, followed by shear failure of the bottom and middle bolts; and bottom flange fracture that started at the weld access hole and propagated across the flange width and thickness, see Fig. 4b [32]. The results shown in Fig. 4 demonstrate the validity of the calibrated fracture parameters for A992 steel and A490 bolts.
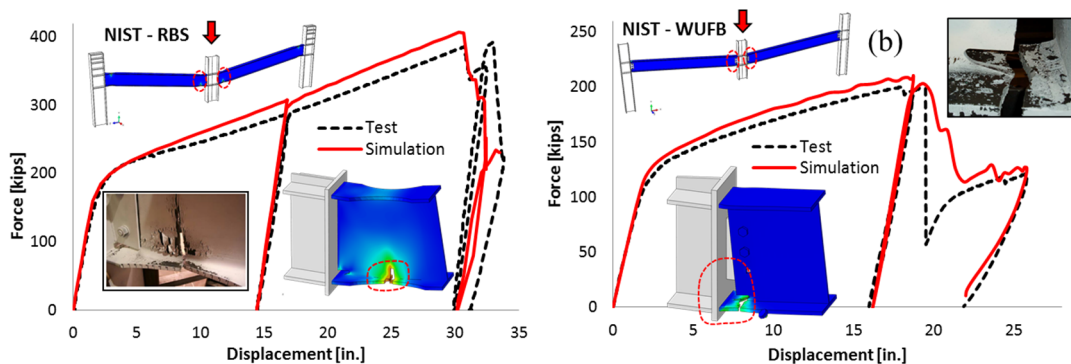

Figure 4. Load-deformation responses and fracture patterns for RBS (a) and WUFB (b) frames.

Steel Moment Connections Subjected to Cyclic Loading

Quasi-static cyclic tests of two steel moment connections were used to validate the cyclic fracture model. The first connection has a beam with reduced section (RBS) welded all around to the column flange [33] and it was loaded using a near-fault cyclic loading protocol proposed in [34]. The beam and columns were all A572 Grade 50 steel, and electrodes E70T6 and E71T8 were used for the flange to column and web to column welds. Fracture started at one edge of the bottom flange at the RBS, then propagated through the thickness and across half of the flange [33]. The

simulated load-deformation response shows good correlation with the test with fracture occurring at the same location and cycle as observed experimentally, see Fig. 5a

The second connection also included a beam with reduced section (A992 Grade 50) welded to an end-plate (A572 Grade 50) that was then bolted to the column [35]. No mention of the electrode types used is made in the report, however weld fractures were not observed for the specimen considered. The material properties for E70T6 were used in the analysis. The AISC 341-10 [36] loading protocol was used to load the specimen. Fracture started in the local buckles tension side at both bottom and top flanges, which later propagated through the flange thickness and width. Through width and thickness top flange fracture and severe tearing at the bottom flange underside happened towards the end of the test. The reversed was observed in the simulation, bottom flange fracture and severe top flange tearing happened, see Fig. 5b. The simulated load-deformation response resembles very well the experimental one.
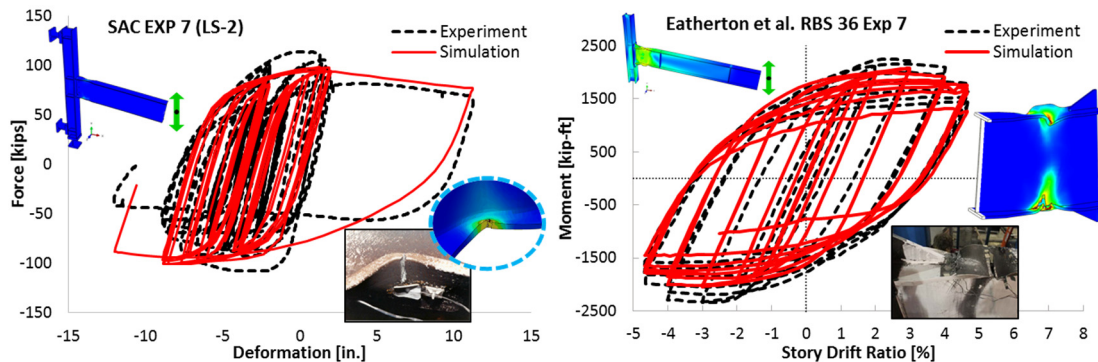

Figure 5. Cyclic responses and fracture patterns for two steel moment connections with RBS.

Shear Link in Steel Eccentric Braced Frame

The last validation example is extracted from the tests performed by Galvez [37], which aim was to study the response of the shear link in eccentrically braced frames (EBF). The test selected corresponds to specimen 9 in [37] and consists of a shear link with stiffeners welded to the flanges and both sides of the web. All elements were A992 Grade 50 steel and welding was done using E70T6 electrodes. The loading protocol for testing EBF links from [38] was used to load the specimen. Failure started with cracks appearing at the top and bottom termination of the weld that joined the web to the stiffeners close to the link ends [37]. Fracture initiation at these locations is attributed to the lower ductility of the material surrounding the weld caused by the welding process. Fracture progressed parallel to the web-to-stiffener welds and parallel to the flanges in the two inside panels. This fracture progression as well as the load-deformation were captured very well in the simulations, see Fig.6. The results demonstrate the validity of the calibrated fracture parameters for A992 steel and the HAZ material.

Conclusions

In this paper a new cyclic fracture model for steel structural components and structures was proposed. The model couples the Yoshida-Uemori plasticity model with a damage model to simulate the softening of the stress-strain response caused by the fracture. An element deletion strategy is used to simulate the fracture propagation. The validation results highlight the model capabilities to capture the global behavior including fracture in in small and large scale steel structural components. The study also highlights the need to include all details relevant, such as the weld details and HAZ, for accurate simulations of the fracture initiation and propagation. The proposed framework provides a robust tool for simulating three-dimensional steel structures

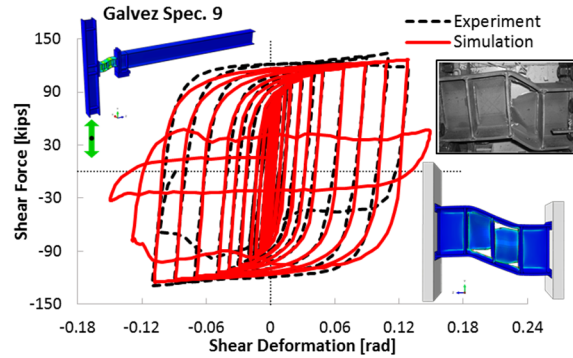subjected to extreme loads that could lead to collapse triggered by fracture in components and connections.

Figure 6. Cyclic response and fracture pattern for EBF shear link with welded stiffeners.

Table 1. Material properties used for validation examples.

Validation Test	Material	σ_y [ksi]	C	B/σ_y	R_{sat}/σ_y	b/σ_y	m	m_l/σ_y	h	$\bar{\varepsilon}_L$	c_1	c_2	$\bar{\varepsilon}_o$	c_3	c_4	γ
CT [27]	A572	48.00	83.06	1.03	0.42	0.00	43.70	1.53	1.00	0.000	20.86	1.68	1.18	-0.90	9.86	-0.40
PL-BH [27]	A572	57.01	83.06	1.16	0.55	0.00	43.70	1.30	1.00	0.006	20.86	1.68	1.18	-0.90	9.86	-0.40
NIST WUFB [32]	A992	53.00	83.06	1.12	0.45	0.00	33.70	1.01	1.00	0.006	15.63	1.48	0.80	-1.11	9.85	-0.46
	A490	98.42	161.47	1.57	0.22	0.00	63.70	0.55	1.00	0.018	20.86	1.80	0.69	-0.90	9.86	1.19
	E70T6	69.62	83.06	1.10	0.24	0.00	21.86	0.52	1.00	0.000	-12.20	1.71	1.07	-0.89	7.69	-0.39
NIST RBS [32]	A992	51.00	83.06	1.36	0.46	0.00	33.70	0.85	1.00	0.006	15.63	1.48	0.80	-1.11	9.85	-0.46
	E70T6	69.62	83.06	1.10	0.24	0.00	21.86	0.52	1.00	0.000	-12.20	1.71	1.07	-0.89	7.69	-0.39
RBS7 [35]	A992	45.00	83.06	1.00	0.17	0.29	24.52	1.23	1.00	0.013	18.63	1.27	1.19	-0.76	9.33	-0.25
	E70T6	69.62	83.06	1.10	0.24	0.00	21.86	0.52	1.00	0.000	-12.20	1.71	1.07	-0.89	7.69	-0.39
LS2 [33]	A572	54.00	83.06	1.04	0.56	0.00	33.70	1.54	1.00	0.006	20.86	1.68	1.18	-0.90	9.86	-0.40
	E70T6	69.62	83.06	1.10	0.24	0.00	21.86	0.52	1.00	0.000	-12.20	1.71	1.07	-0.89	7.69	-0.39
	E71T8K6	81.62	83.06	1.07	0.19	0.00	21.86	0.78	1.00	0.000	-12.20	1.71	1.07	-0.89	7.69	-0.39
Spec.9 [37]	A992	50.87	83.06	1.31	0.44	0.10	5.60	0.64	1.00	0.023	13.74	1.97	1.19	-0.76	9.33	-0.25
	HAZ	50.87	83.06	1.31	0.44	0.10	5.60	0.64	1.00	0.023	18.16	1.97	0.95	-0.76	9.33	-0.25
	E70T6	69.62	83.06	1.10	0.24	0.00	21.86	0.52	1.00	0.000	-12.20	1.71	1.07	-0.89	7.69	-0.39

[1]The fracture energy for all material listed is $G_{fo} = 5.46 \times 10^{-3}$ [ksi/in.]

References

1. Almar-Naess, A., Haagensen, P., Lian, B., Moan, T., Simonsen, T., "Investigation of the Alexander L. Kielland failure-Metallurgical and fracture analysis." *J. Energy Resour. Technol*. 1984, 106(1), 24–31.
2. Cooper, J., Friedland, I., Buckle, I., Nimis, R., Bobb, N., *The Northridge Earthquake: Progress Made, Lessons Learned in Seismic-Resistant Bridge Design*, 58, U.S.DOT FHWA, Washington, D.C., 1994.
3. Miyazaki, Y., Abe, K., Ando, M., Ishida, M., and et al., *Seismic activity in Japan*, Nov. 11, 2017, http://www.hp1039.jishin.go.jp/eqchreng/eqchrfrm.htm.
4. Bai, Y., and Wierzbicki, T., "A new model of metal plasticity and fracture with pressure and Lode dependence."

International Journal of Plasticity 2008, 24(6), 1071–1096.

5. Wen, H., and Mahmoud, H., "New Model for Ductile Fracture of Metal Alloys. I: Monotonic Loading." *Journal of Engineering Mechanics* 2016, 142(2), 04015088.

6. Kanvinde A., and Deierlein G., "Cyclic Void Growth Model to Assess Ductile Fracture Initiation in Structural Steels due to Ultra Low Cycle Fatigue." *Journal of Engineering Mechanics* 2007, 133(6), 701–712.

7. Yoshida, F., and Uemori, T., "A model of large-strain cyclic plasticity describing the Bauschinger effect and work hardening stagnation." *International Journal of Plasticity* 2002, 18(5), 661–686.

8. Jia, L.-J., and Kuwamura, H., "Prediction of cyclic behaviors of mild steel at large plastic strain using coupon test results." *Journal of Structural Engineering* 2014, 140(2), 04013056.

9. Lemaitre, J., and Chaboche, J.-L., *Mechanics of Solid Materials*. Cambridge University Press, 1990.

10. Xue, L., "Damage accumulation and fracture initiation in uncracked ductile solids subject to triaxial loading." *International Journal of Solids and Structures* 2007, 44(16), 5163–5181.

11. Wen, H., and Mahmoud, H., "New model for ductile fracture of metal alloys II: Reverse loading." *Journal of Engineering Mechanics* 2016, 142(2).

12. Hillerborg, A., Modeer, M., and Petersson, P.E., "Analysis of crack formation and crack growth in concrete by means of fracture mechanics and finite elements." *Cement and Concrete Research* 1976, 6(6), 773-782.

13. Zaverl, F., Lee, D., "Constitutive relations for nuclear reactor core materials" *Journal of Nuclear Materials* 1978, 75(1), 14–19.

14. Ohno, N., "A constitutive model of cyclic plasticity with a nonhardening strain region." *Journal of Applied Mechanics* 1982, 49(4), 721–727.

15. Bai, Y., *Effect of loading history in necking and fracture*, Ph.D. dissertation, Massachusetts Institute of Technology, Cambridge, MA, 2008.

16. Bai, Y., and Wierzbicki, T., "Application of extended Mohr–Coulomb criterion to ductile fracture." *International Journal of Fracture* 2009, 161(1), 1–20.

17. Xue, L., Wierzbicki, T., "Ductile fracture initiation and propagation modeling using damage plasticity theory." *Engineering Fracture Mechanics* 2008, 75(11), 3276–3293.

18. Cao, T.S., Gachet, J.M., Montmitonnet, P., Bouchard, P.O., "A Lode-dependent enhanced Lemaitre model for ductile fracture prediction at low stress triaxiality." *Engineering Fracture Mechanics* 2014, 124–125, 80–96.

19. Cockcroft, M., Latham, D., "Ductility and the workability of metals." *J. Inst. Metals* 1968, 96(1), 33–39.

20. Brozzo, P., Deluca, B., and Rendina, R., "A new method for the prediction of formability limits in metal sheets, sheet metal forming and formability." *Proc., 7th Biennial Conf. of the Int. Deep Drawing Research Group* 1972, International Deep Drawing Research Group, Netherlands.

21. Oh, S. I., Chen, C. C., and Kobayashi, S., "Ductile fracture in axisymmetric extrusion and drawing—Part 2: Workability in extrusion and drawing." *J. Eng. Ind.* 1979, 101(1), 36–44.

22. Bao, Y., and Wierzbicki, T., "On the cut-off value of negative triaxiality for fracture." *Engineering Fracture Mechanics* 2005, 72(7), 1049–1069.

23. Smith, C., Deierlein, G., Kanvinde, A., *A Stress-Weighted Damage Model for Ductile Fracture Initiation in Structural Steel Under cyclic Loading and Generalized Stress States*. John A. Blume Earthquake Engineering Technical Report 187. Stanford Digital Repository, 2014.

24. Khan, A., Liu, H., "A new approach for ductile fracture prediction on Al 2024-T351 alloy." *International Journal of Plasticity* 2012, 35(Supplement C), 1–12.

25. Mae, H., Teng, X., Bai, Y., Wierzbicki, T., "Calibration of ductile fracture properties of a cast aluminum alloy." *Materials Science and Engineering: A* 2007, 459(1), 156–166.

26. ABAQUS 6.14, *Abaqus User Manual*, Simulia, Dassault Systèmes, Providence, RI, 2014.

27. Kanvinde, A., Deierlein, G., *Micromechanical Simulation of Earthquake-Induced Fracture in Steel Structures*. John A. Blume Earthquake Engineering Center Technical Report 145. Stanford Digital Repository, 2004.

28. Myers, A., Deierlein, G., Kanvinde, A., *Testing and Probabilistic Simulation of Ductile Fracture Initiation in Structural Steel Components and Weldments*. John A. Blume Earthquake Engineering Center Technical Report 170. Stanford Digital Repository, 2013.

29. Deng, K., Grondin, G.Y., Driver, R.G., "*Effect of Loading Angle on the Behavior of Fillet Welds*", Dept. of Civil & Environmental Engineering Structural Engineering Report 251, University of Alberta, 2003.

30. Ng, A., Driver, R.G., Grondin, G.Y., "*Behaviour of transverse fillet welds*", Dept. of Civil & Environmental Engineering Structural Engineering Report 245, University of Alberta, 2002.

31. Kulak, G., Fisher, J., Struik, J., *Guide to Design Criteria for Bolts and Riveted Joints*, 2nd Ed., John Wiley & Sons, New York, 1986.

32. Sadek, F., Main, J., Lew, H., Robert, S., Chiarito, V., El-Tawil, S., *An Experimental and Computational Study of Steel Moment Connections under a Column Removal Scenario*, NIST Technical Note 1669, NIST, U.S. Department of Commerce, Gaithersburg, Maryland, 2010.

33. SEAOC, ATC, CUREE, "*SAC Steel Project Database*," Network for Earthquake Engineering Simulation (database), Dataset, DOI:10.4231/D3FQ9Q536, 2011.

34. Clark, P., Frank, K., Krawinkler, H., Shaw, R., "*Protocol for Fabrication, Inspection, Testing, and*

Documentation of Beam-Column Connection Tests and Other Experimental Specimens." Report No. SAC/BD-97/02, SAC Joint Venture, Sacramento, CA, 1997.

35. Eatherton, M., Toellner, B., Watkins, C., and Abbas, E., "*The Effect of Powder Actuated Fasteners on the Seismic Performance of Protected Zones in Steel Moment Frames*", Virginia Tech SEM Report Series, Report No. CE/VPI-ST-13/05; 2014.

36. AISC. ANSI/AISC 341-10, *Seismic provisions for structural steel buildings*. Chicago, IL, AISC, 2010.

37. Galvez P. *Investigation of factors affecting web fractures in shear links*. Master's thesis, University of Texas at Austin, Austin, TX, USA, 2004.

38. AISC, ANSI/AISC 341-05, *Seismic provisions for structural steel buildings*, Chicago, IL, AISC, 2005.